AFRL-RX-WP-JA-2016-0194

QUANTITATIVE VOXEL-TO-VOXEL COMPARISON OF TRIBEAM AND DCT STRONTIUM TITANATE THREE-DIMENSIONAL DATA SETS (POSTPRINT)

William C. Lenthe, McLean P. Echlin, and Tresa M. Pollock
University of California at Santa Barbara

Andreas Trenkle, Melanie Syha, and Peter Gumbsch
Karlsruhe Institute of Technology

Melanie Syha
European Synchrotron Radiation Facility

Peter Gumbsch
Fraunhofer IWM

9 FEBRUARY 2015
Interim Report

(STINFO COPY)

AIR FORCE RESEARCH LABORATORY
MATERIALS AND MANUFACTURING DIRECTORATE
WRIGHT-PATTERSON AIR FORCE BASE, OH 45433-7750
AIR FORCE MATERIEL COMMAND
UNITED STATES AIR FORCE

REPORT DOCUMENTATION PAGE

Form Approved
OMB No. 0704-0188

1. REPORT DATE *(DD-MM-YY)*	2. REPORT TYPE	3. DATES COVERED *(From - To)*
9 February 2015	Interim	13 July 2013 – 9 January 2015

4. TITLE AND SUBTITLE	5a. CONTRACT NUMBER
QUANTITATIVE VOXEL-TO-VOXEL COMPARISON OF TRIBEAM AND DCT STRONTIUM TITANATE THREE-DIMENSIONAL DATA SETS (POSTPRINT)	FA8650-10-D-5226-0003

5b. GRANT NUMBER

5c. PROGRAM ELEMENT NUMBER
62102F

6. AUTHOR(S)	5d. PROJECT NUMBER
1) William C. Lenthe, McLean P. Echlin, and Tresa M. Pollock - University of California 2) Andreas Trenkle, Melanie Syha, and Peter Gumbsch - KIT (continued on pg. 2)	4347

5e. TASK NUMBER   0003

5f. WORK UNIT NUMBER
X0LX

7. PERFORMING ORGANIZATION NAME(S) AND ADDRESS(ES)	8. PERFORMING ORGANIZATION REPORT NUMBER
Materials Department, University of California at Santa Barbara, Mesa Rd, Santa Barbara, CA 93106-5050 Karlsruhe Institute of Technology (KIT), Kaiser Street 12, 76131 Karlsruhe, Germany (Continued on page 2)	

9. SPONSORING/MONITORING AGENCY NAME(S) AND ADDRESS(ES)	10. SPONSORING/MONITORING AGENCY ACRONYM(S)
Air Force Research Laboratory Materials and Manufacturing Directorate Wright-Patterson Air Force Base, OH 45433-7750 Air Force Materiel Command United States Air Force	AFRL/RXCCM

11. SPONSORING/MONITORING AGENCY REPORT NUMBER(S)
AFRL-RX-WP-JA-2016-0194

12. DISTRIBUTION/AVAILABILITY STATEMENT
Distribution Statement A. Approved for public release: distribution unlimited.

14. ABSTRACT *(Maximum 200 words)*
Recently, techniques for the acquisition of three-dimensional tomographic and four-dimensional time-resolved data sets have emerged, allowing for the analysis of mm3 volumes of material with nm-scale resolution. The ability to merge multi-modal data sets acquired via multiple techniques for the quantitative analysis of structure, chemistry and phase information is still a significant challenge. Large three-dimensional data sets have been acquired by time-resolved diffraction contrast tomography (DCT) and a new TriBeam tomography technique with high spatial resolution to address grain growth in strontium titanate. A methodology for combining three-dimensional tomographic data has been developed. Algorithms for the alignment of orientation reference frames, unification of sampling grids and automated grain matching have been integrated, and the resulting merged data set permits the simultaneous analysis of all tomographic data on a voxel-by-voxel and grain-by-grain basis.

15. SUBJECT TERMS

diffraction contrast tomography; strontium titanate; electron backscatter diffraction; TriBeam; femtosecond lasers

16. SECURITY CLASSIFICATION OF:			17. LIMITATION OF ABSTRACT:	18. NUMBER OF PAGES	19a. NAME OF RESPONSIBLE PERSON (Monitor)
a. REPORT Unclassified	b. ABSTRACT Unclassified	c. THIS PAGE Unclassified	SAR	16	Patrick Carlin 19b. TELEPHONE NUMBER *(Include Area Code)* (937) 255-9800

Standard Form 298 (Rev. 8-98)
Prescribed by ANSI Std. Z39-18

REPORT DOCUMENTATION PAGE Cont'd

6. AUTHOR(S)

    3) Melanie Syha - ESRF

    4) Peter Gumbsch - Fraunhofer IWM

7. PERFORMING ORGANIZATION NAME(S) AND ADDRESS(ES)

    3) European Synchrotron Radiation Facility,
        CS 40220 71, Avenue des Martyrs,
        38043 Grenoble, France

    4) Fraunhofer IWM, Woelerstr. 11, 79108 Freiburg,
        Germany

research papers

CrossMark

Quantitative voxel-to-voxel comparison of TriBeam and DCT strontium titanate three-dimensional data sets

William C. Lenthe,[a]* McLean P. Echlin,[a] Andreas Trenkle,[b] Melanie Syha,[b,c] Peter Gumbsch[b,d] and Tresa M. Pollock[a]

[a]Materials Department, University of California – Santa Barbara, Santa Barbara, CA 93106-5050, USA, [b]Institute for Applied Materials IAM, Karlsruhe Institute of Technology (KIT), Germany, [c]European Synchrotron Radiation Facility, 38000 Grenoble, France, and [d]Fraunhofer IWM, Freiburg, Germany. *Correspondence e-mail: wlenthe@engineering.ucsb.edu

Recently, techniques for the acquisition of three-dimensional tomographic and four-dimensional time-resolved data sets have emerged, allowing for the analysis of mm^3 volumes of material with nm-scale resolution. The ability to merge multi-modal data sets acquired *via* multiple techniques for the quantitative analysis of structure, chemistry and phase information is still a significant challenge. Large three-dimensional data sets have been acquired by time-resolved diffraction contrast tomography (DCT) and a new TriBeam tomography technique with high spatial resolution to address grain growth in strontium titanate. A methodology for combining three-dimensional tomographic data has been developed. Algorithms for the alignment of orientation reference frames, unification of sampling grids and automated grain matching have been integrated, and the resulting merged data set permits the simultaneous analysis of all tomographic data on a voxel-by-voxel and grain-by-grain basis. Quantitative analysis of merged data sets collected using DCT and TriBeam tomography shows that the spatial resolution of the DCT technique is limited near grain boundaries and the sample edge, resolving grains down to 10 μm diameter for the reconstruction method used. While the TriBeam technique allows for higher-resolution analysis of boundary plane location, it is a destructive tomography approach and can only be employed at the conclusion of a four-dimensional experiment.

1. Background

Advances in nondestructive synchrotron-based tomography techniques such as X-ray diffraction contrast tomography (DCT) (Poulsen *et al.*, 2001; Reischig *et al.*, 2013) have led to new insights on grain growth mechanisms (Gonzalez *et al.*, 2013) *via* acquisition of spatial grain orientation information at multiple time steps using four-dimensional microscopy. However, synchrotron tomography reconstruction algorithms (Poulsen *et al.*, 2001; Ludwig *et al.*, 2008) for diffraction-based synchrotron data sets have low confidence in spatial resolution near grain boundaries. Recent data-set reconstruction algorithm developments have improved the resolution of these techniques (Schmidt, 2014) and combined near- and far-field experiments have validated grain orientation indexing (Nervo *et al.*, 2014). However, DCT reconstruction algorithms lack a reference data set for direct analysis. Ultrashort pulse laser based techniques for serial sectioning and three-dimensional reconstruction have been recently developed (Echlin *et al.*, 2012; Echlin, Mottura *et al.*, 2014). The TriBeam system couples a femtosecond laser with a dual-beam focused ion beam (FIB) scanning electron microscope enabling rapid *in*

100 μm

situ collection of structural, chemical and topological information. Although destructive, TriBeam and similar methods allow for interrogation with a higher spatial resolution in all three dimensions. Other existing serial sectioning techniques combined with electron backscatter diffraction (EBSD) may achieve high resolution in the imaging plane, but do not allow similar resolution in all dimensions. Mechanical polishing techniques were previously applied to compare DCT with individual section cuts (Syha *et al.*, 2013) but required laborious hand matching. In this work we present methods for direct grain and voxelmetric comparisons of full volumetric three-dimensional data sets including orientation data. We apply these methods to strontium titanate (STO) data sets that were collected with the TriBeam and DCT techniques over the same volume within a single sample.

2. Methodology

The STO sample used in this study was prepared *via* the mixed-oxide synthesis route from $SrCO_3$ and TiO_2 powders with an Sr/Ti ratio of 0.996. The powders were calcined, undergoing the solid-state reaction

$$SrCO_3 + TiO_2 \rightarrow SrTiO_3 + CO_2. \tag{1}$$

The resulting $SrTiO_3$ powder was pressed and sintered for 1 h at 1873 K in an oxygen atmosphere, then ground to a cylindrical pedestal of 320 µm diameter. More details of the processing route are available elsewhere (Syha, Rheinheimer *et al.*, 2012; Bäurer, Weygand *et al.*, 2009; Bäurer, Kungl *et al.*, 2009). The sample was annealed for another hour at 1873 K to encourage grain growth. The sample was imaged with the DCT technique (Syha, Rheinheimer *et al.*, 2012; Syha, Bäurer *et al.*, 2012) before and after the thermal annealing cycle at the

materials science beamline ID11 of the European Synchrotron Radiation Facility and subsequently with TriBeam tomography.

2.1. Experimental data collection

Data sets were gathered from a single cylindrical pedestal sample of STO using DCT and TriBeam tomography. The DCT data sets used in this research were reconstructed and presented previously (Syha, Rheinheimer *et al.*, 2012), so details of these methods are only briefly summarized. This work focuses on the direct merger of a DCT reconstruction with a TriBeam data set; implications for grain growth will be covered in a subsequent paper. Experimental conditions used for acquisition will be discussed in the next two sections.

2.1.1. DCT data collection. X-ray DCT is a nondestructive three-dimensional tomography technique for imaging crystalline microstructures and the reconstruction of grain shape and orientation (Poulsen *et al.*, 2001; Ludwig *et al.*, 2008; Johnson *et al.*, 2008; Ludwig, Reischig *et al.*, 2009). The sample is incrementally rotated through 360° while being exposed to a parallel monochromatic X-ray beam. The diffraction intensities for crystals that fulfill the Bragg condition, $\lambda n = 2d \sin \theta$, are detected on a screen. A schematic of the experimental setup is shown in Fig. 1.

Two DCT data sets were collected from an STO sample using the DCT technique (Syha, Rheinheimer *et al.*, 2012). The final data set contains phase contrast and diffraction contrast data and will be the focus of this work. Diffraction information was collected every 0.05° with a 0.7 µm pixel size detector at 36 keV using a sample-to-detector distance of 3.23 mm. An annealing heat treatment was performed at 1873 K for 1 h between DCT data-set collections. The phase, absorption and diffraction contrast data were reconstructed using algorithms that are described elsewhere (Reischig *et al.*, 2013; Kak & Slaney, 1988; Johnson *et al.*, 2008; Cloetens *et al.*, 1997), and have been used to reconstruct grain information in materials such as alumina (Gonzalez *et al.*, 2013), titanium (King *et al.*, 2010) and aluminium (Ludwig, King *et al.*, 2009).

2.1.2. TriBeam data collection. After the final thermal cycling and DCT data-set collection, the strontium titanate sample was destructively sectioned using the TriBeam system for three-dimensional EBSD data collection. This technique has been applied to materials such as CuW composites (Echlin *et al.*, 2012), titanium and nickel alloys (Echlin, Lenthe *et al.*, 2014), and geological samples (Echlin *et al.*, 2015). The strontium titanate sample was serially sectioned in the TriBeam system by femtosecond laser ablation for layer-
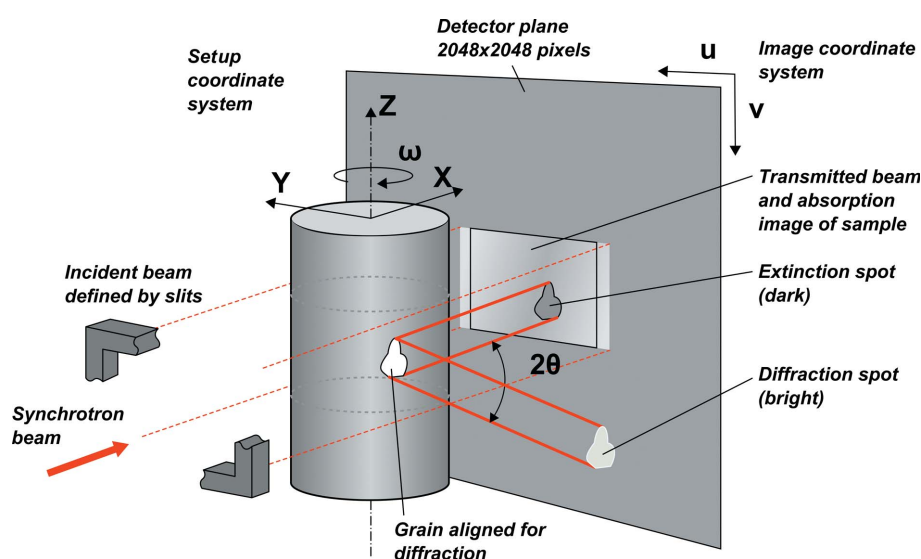

Figure 1
X-ray DCT experiments are performed by irradiating a sample with a beam defined by apertures or slits in the beamline. The sample is rotated in increments of $\omega = 0.05°$, around the *z* axis. Extinction and diffraction spots simultaneously appear and disappear on the transmitted-beam region of the detector (center of detector) and in the surrounding area (diffraction spots). Figure reproduced after Ludwig, Reischig *et al.* (2009).

William C. Lenthe *et al.* · Comparison of TriBeam and DCT STO data sets **1035**

by-layer EBSD analysis with the laser beam scanned parallel to the sample surface. Material was removed with the femtosecond laser at a rate of 1 µm per slice, which is controlled by the distance the sample is raised into the beam by a piezoelectric stage as shown in Fig. 2. For each slice, the laser-machined sample surface was ion milled at a 21° glancing angle using a 30 kV, 30 nA Ga^+ ion beam to a depth of ~100 nm and then with a 5 kV, 13 nA beam to a depth of ~50 nm, improving the EBSD pattern quality on the femtosecond laser machined surface by reducing the surface roughness and lowering dislocation density within several hundred nanometres below the sample surface (Echlin et al., 2015; Titus et al., 2015). EBSD data were collected using an EDAX Hikari XP detector with a 1 µm step size and a 25 kV electron beam in a 4×4 camera binning mode. The EBSD data collection parameters were optimized for speed, therefore limiting the angular resolution in exchange for optimization of the data collection time and spatial resolution of the scans.

2.2. Data-set reconstruction

The two tomographic techniques employed collect diffraction information in fundamentally different modes. DCT collects projections from all grains with orientations satisfying the Bragg condition simultaneously. In contrast, EBSD patterns are collected serially for each voxel in the TriBeam experiment. Therefore, each technique requires a different three-dimensional reconstruction method.

2.2.1. DCT data reconstruction. The DCT data sets were reconstructed using a crystallographic indexing scheme that was adapted to perovskite materials (Ludwig, Reischig et al., 2009). Spatial grain information was reconstructed using the algebraic reconstruction technique (Kak & Slaney, 1988). A uniform morphological dilation procedure was used to create a space-filling model of the grain structure (Syha et al., 2013). Phase contrast information was also captured during the DCT experiment and was coupled with the space-filling model to account for porosity. A detailed description of the DCT reconstruction can be found elsewhere (Syha, Rheinheimer et al., 2012).

2.2.2. TriBeam data reconstruction. The raw data produced during this TriBeam experiment consist of a series of EBSD images (70° tilt angle), scanning electron microscopy (SEM) images (0° tilt angle) and high-resolution stage encoder data. Spatial distortions may be present during electron imaging owing to drift and electron optics (Sutton et al., 2006;
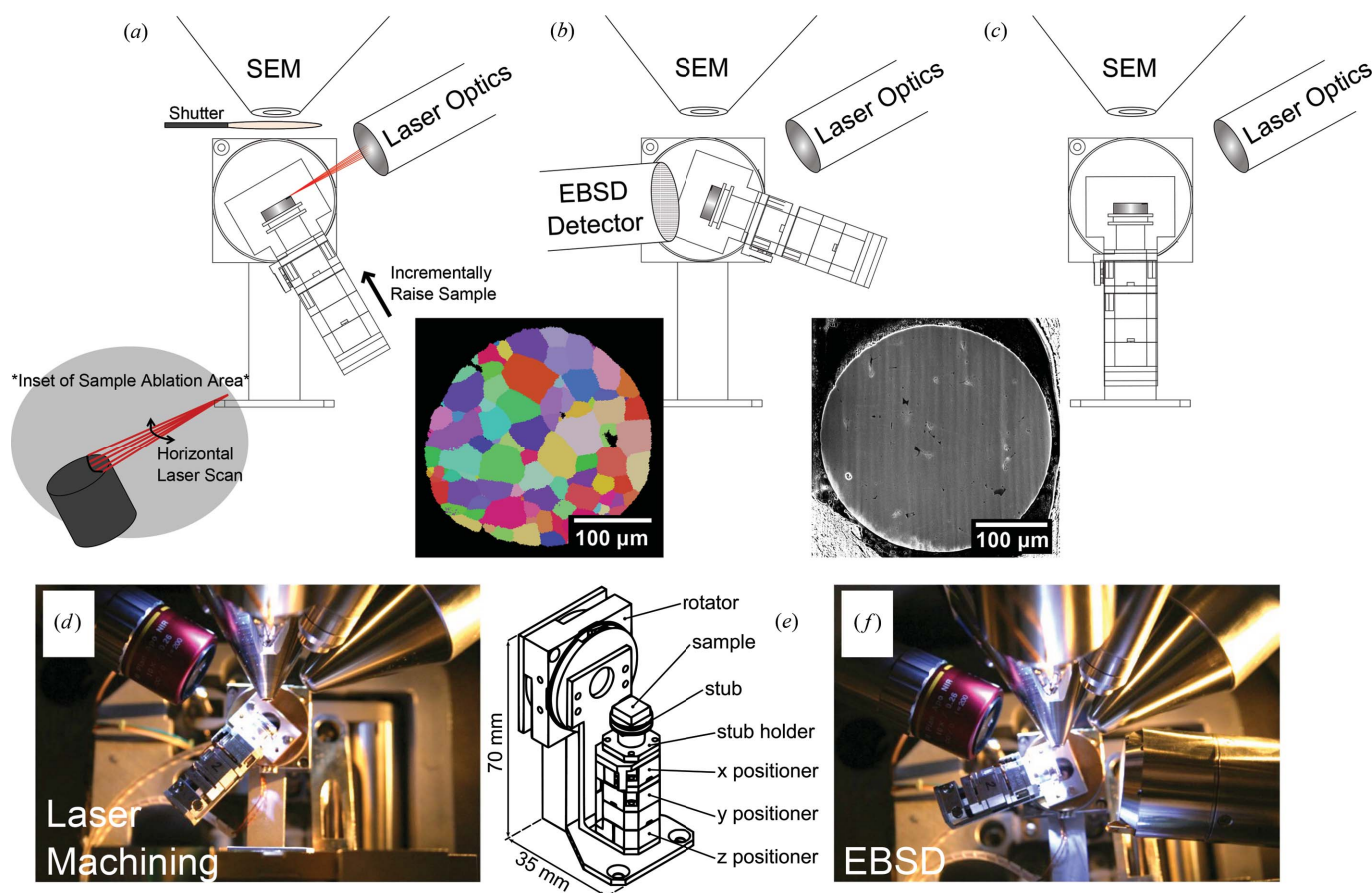

Figure 2
TriBeam experiments use a high-precision piezoelectric stage to position the sample within the microscope chamber. (a) The sample is tilted to 30° for surface parallel femtosecond laser ablation. The laser is scanned horizontally across the sample surface to remove the material which has been incrementally raised into the focused beam path. (b) The piezoelectric stage is tilted for EBSD data collection (70°) with the detector inserted. (c) The sample is tilted to 0° for SEM imaging. Photographs of configurations (a) and (b) are shown in (d) and (f), respectively. (e) A schematic of the piezoelectric stack with components labeled is shown.

Kammers & Daly, 2013; Stinville *et al.*, 2015), and during EBSD acquisition owing to tilt correction (Nolze, 2007; Rowenhorst, 2013). Geometric and drift distortions are limited by the use of high-precision piezoelectric stages; however nonlinear lens distortions were not addressed. Instrument-specific distortions can be addressed within the data-set alignment framework presented here, although this is not the focus of this work because the distortion fields will be unique to each instrument and corresponding approach to data collection. During the TriBeam experiment, the femtosecond laser cut angle was consistently 5° off from parallel with the face of the sample pedestal, so a tilt correction was applied to the EBSD scans. *DREAM.3D* (Groeber & Jackson, 2014) was used for subsequent three-dimensional reconstruction of the EBSD data using the data processing steps detailed in the supporting information and outlined below. The EBSD scans were stacked into a three-dimensional data container with rotations of 180° about [010] and 90° about [001] applied to the sample and orientation reference frames, respectively, to account for manufacturer definitions. A mask was applied to define the boundary of the sample pedestal by

thresholding voxels with a confidence index greater than 0.01 and an image quality (Wright & Nowell, 2006) greater than 200. The mask was dilated to fill in all pores and include pedestal edge data. EBSD slices were aligned along the **z** direction by maximizing voxels within a 5° disorientation angle tolerance (relative to the previous slice). Grains were defined from the aligned data set using a 1.5° segmentation tolerance. Grains below 125 voxels in size or having fewer than three neighbors were removed and surrounding grains dilated in order to restrict the analysis to only grains which were substantially above the spatial resolution (step size) of the EBSD data collected.

2.3. Data merging

Two data sets sharing a common volume typically have different orientation reference frames (the coordinate system in which orientations are expressed) and sampling grids. In this state only ensemble properties, such as grain size distribution, can be compared. To facilitate direct quantitative comparisons on a grain and voxel scale, the two data sets must have their orientation reference frames aligned and be merged onto a single shared sampling grid. To align the data sets several matching grain pairs are manually identified for the initial coarse alignment. Grain-pair centroids and average orientations are used to align the data-set sampling grids and orientation reference frames, respectively. Grain pairs are next automatically identified in the coarsely aligned volume. These steps are repeated until no new grain pairs are identified, as represented in an outline of the merging process depicted in Fig. 3. The transformations from all loop iterations are combined and the total transformation is applied to the original volume to avoid generation of artifacts from repeated nearest-neighbor interpolation, shown in Fig. 4. The details of each step in this iterative data-set merging framework are provided in §§2.3.1–2.3.4.
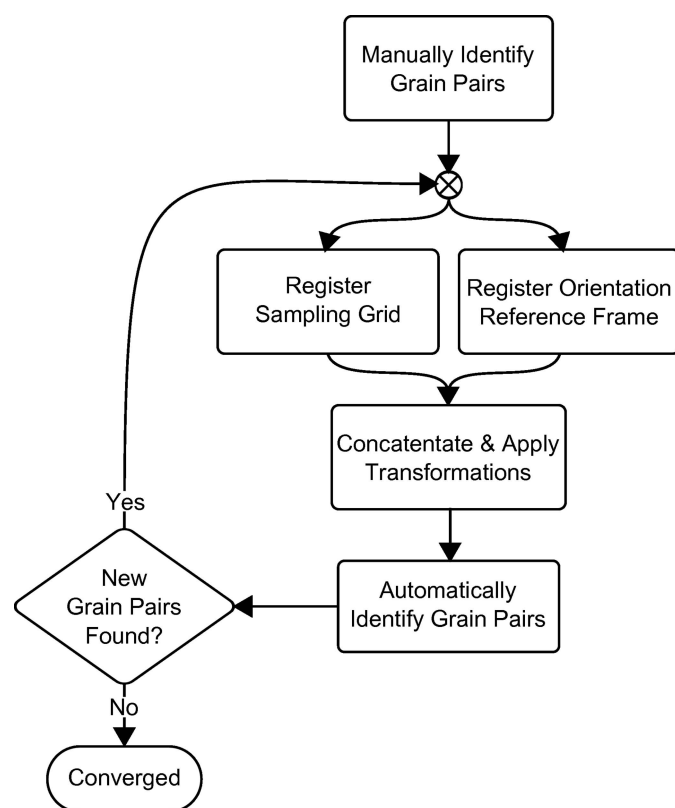
Figure 3
A flow chart outlining the alignment process with boxes representing algorithms and diamonds representing a loop condition is shown. A set of grain pairs is identified to initialize the alignment loop. The transformations necessary to align the sampling grids and orientation reference frames are computed independently. The data sets are then coarsely aligned, enabling automatic identification of matching grain pairs. Since grain pairs are the input for computation of both transformations, the alignment has converged when no new pairs are identified. The algorithms used in this workflow for registration could easily be replaced or modified to accept various other data or feature types for alignment.
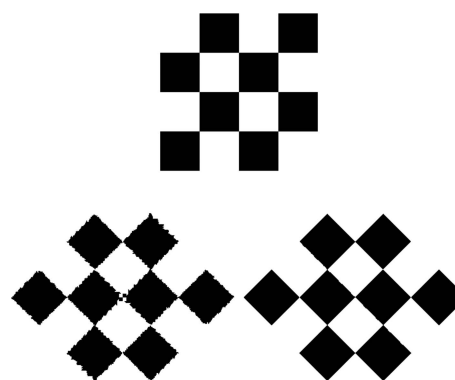
Figure 4
An example of artifacts introduced by repeated interpolation is shown. In nearest-neighbor interpolation the value of each pixel in the resampled image is taken from the closest pixel in the transformed image. The original image (top) was rotated by 45° in 5° increments with nearest-neighbor interpolation resulting in extensive artifacts (bottom left). The same transformation introduces comparatively few artifacts when performed in one step (bottom right).
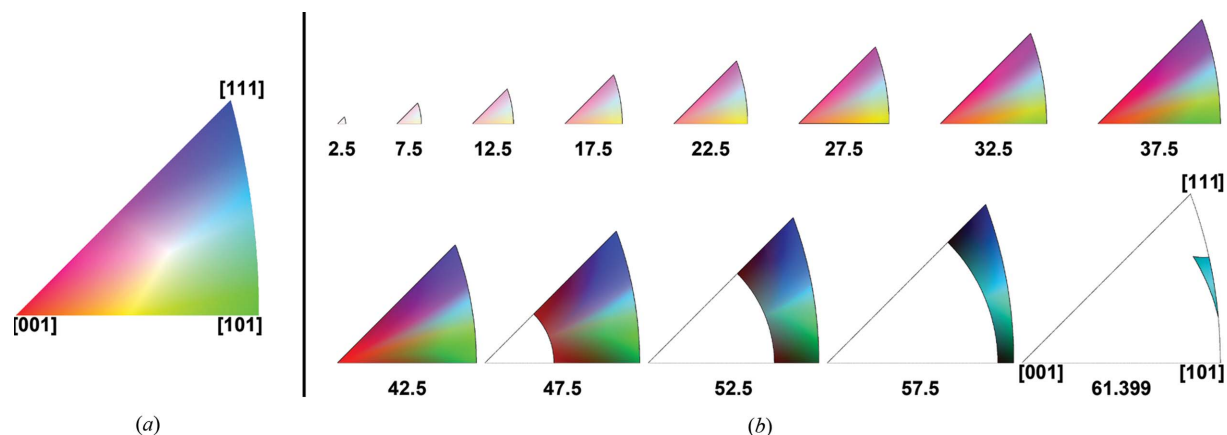
William C. Lenthe *et al.* · Comparison of TriBeam and DCT STO data sets   **1037**

Figure 5
Grain and voxel orientations in this paper are represented with either inverse pole figure (IPF) coloring (*a*) or disorientation coloring (*b*) (Patala *et al.*, 2012). To determine the color to which a disorientation maps, first select the stereographic triangle corresponding to the disorientation angle, then locate the color at the disorientation axis. For example, to identify the disorientation color for 36.86° about [001], select the 37.5° stereographic triangle and locate the color at [001] (red). Disorientation coloring can also be used to color orientations. Orientations are colored by computing the disorientation relative to the reference frame (imposing the symmetry operators of the crystal on the reference frame). The resulting disorientation is then mapped as described above.

Typically, orientation reference frames are defined with respect to the coordinate system of the sampling grid, coupling the transformations required for their alignment. In practice, this coupling may be unknown or nonintuitive since the rotation between sample coordinate systems and orientation reference frames can differ among experimental setups and software environments, *e.g.* EBSD instrument manufacturers. Furthermore, rotations of the orientation reference frame or sampling grid can be introduced into EBSD data by deviation from an ideal collection geometry. An affine transformation can be used to correct linear distortions in the sampling grid that do not exist in the orientation reference frame. Examples of these distortions include errors in magnification calibration (scaling), slice alignment (shear) and sample placement (translation and rotation). Therefore, procedures for the independent alignment of the sampling grid and the orientation reference frame have been developed. When applied in parallel it is expected that each will yield similar transformations in terms of the global rotation of the sample between the two data sets, assuming a consistent orientation reference frame definition.

2.3.1. Manual grain-pair identification. The algorithms used to register the sampling grids and orientation reference frames require pairs of grains matched between the DCT and TriBeam data sets as input. Consequentially, several grain pairs must be manually selected to initialize the alignment loop. In large data sets, pairs may not be readily distinguished by morphology alone and orientation-based coloring will not correlate between data sets with unaligned reference frames. However, grain boundary surface meshes can be colored by their disorientations (Patala *et al.*, 2012), which are relative between crystal reference frames. The legend for the disorientation coloring scheme, along with a brief description of its interpretation, is given in Fig. 5. This mitigates the need for prior orientation reference frame alignment, and grain pairs are readily identified by boundary color as shown in Fig. 6.

2.3.2. Register and align sampling grid. Aligning two sampling grids requires selection of a feature or group of features to make coincident. Grain centroids were chosen as the alignment target since they can be robustly determined by both techniques. Grains not fully contained in both volumes were excluded to avoid bias. The least-squares affine trans-
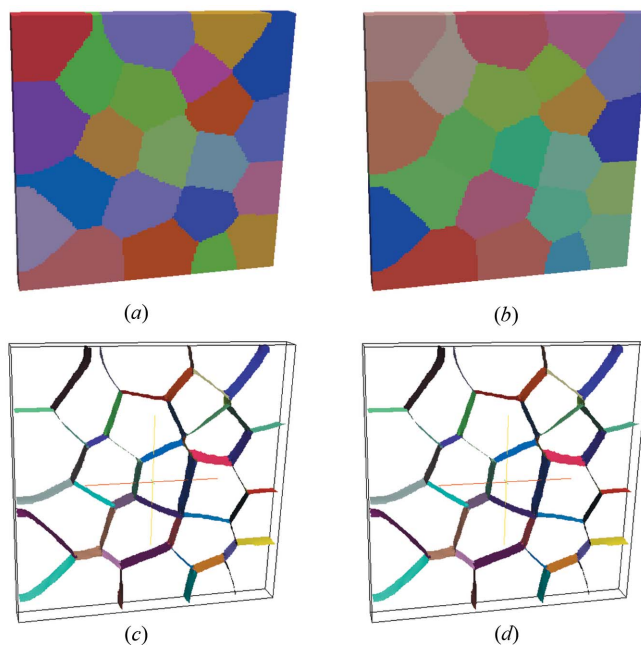

Figure 6
A small synthetic volume (*a*) with IPF coloring is shown. An arbitrary rotation is applied to the orientation reference frame (*b*), altering the IPF colors. A grain boundary surface mesh is generated using the Multi-Material Marching Cubes algorithm and subsequently Laplacian smoothed (Wu & Sullivan, 2003). The mesh is colored by boundary disorientation in the original (*c*) and rotated (*d*) orientation reference frames. Since misorientations are relative in a crystal frame, the coloring is consistent, making identification of matching grains straightforward. Color legends are available in Fig. 5.

5

formation $[T]$ mapping centroids in data set B to those in data set A is computed:

$$[T]_{4x4} = A_{4xn}^{T} B_{nx4} \left(B_{4xn}^{T} B_{nx4} \right)^{-1},$$

$$A = \begin{bmatrix} a_1^x & a_1^y & a_1^z & 1 \\ a_2^x & a_2^y & a_2^z & 1 \\ \vdots & \vdots & \vdots & \vdots \\ a_n^x & a_n^y & a_n^z & 1 \end{bmatrix},$$

$$B = \begin{bmatrix} b_1^x & b_1^y & b_1^z & 1 \\ b_2^x & b_2^y & b_2^z & 1 \\ \vdots & \vdots & \vdots & \vdots \\ b_n^x & b_n^y & b_n^z & 1 \end{bmatrix}, \tag{2}$$

where $(a_i^x,\ a_i^y,\ a_i^z)$ is the centroid of grain i in data set A. A detailed derivation of the least-squares affine transformation is available in the supporting information for this article. The transformation calculation may be easily modified to restrict degrees of freedom or introduce centroid weighting (Gower & Dijksterhuis, 2004), for example the grain volume weighted least-squares similarity transform. To merge both data sets onto a single grid, the transformation is applied to data set B and the transformed volume resampled on the sampling grid of data set A using nearest-neighbor interpolation. A schematic showing the transformation of data set B to the sampling grid of data set A is shown schematically in Fig. 7, with a detailed description provided in Fig. 8.

2.3.3. Register and align orientation reference frame. The rotation between two orientation reference frames cannot be determined by a single orientation pair because of crystal symmetry, as shown in Fig. 9. The rotation between a given pair can be expressed in a different way for each crystal symmetry operator:

$$T_i = g_1 * O_i^{\mathrm{sym}} * g_2^{-1} \tag{3}$$

where T_i is the orientation reference frame transformation, g_1 and g_2 are grain orientations for a matched pair in two different reference frames, and O_i^{sym} are symmetry operators. With multiple grain pairs, each potential rotation can be checked against other pairs to select the permutation resulting in the lowest disorientation angle for all other pairs. To determine the rotation required to align sample reference frames, this procedure is performed for each pair of grains and the resulting rotations averaged as shown in Fig. 10.

2.3.4. Automatic feature matching and iterative alignment. Once a single alignment loop has been completed using manually selected grain pairs, the correspondence is sufficient for automated identification of additional pairs. Volume intersection normalized by total
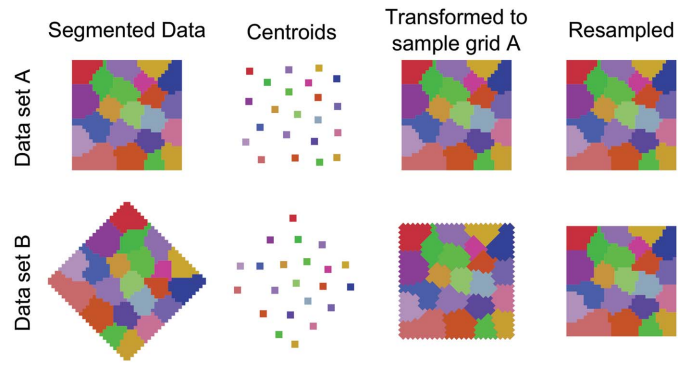

Figure 7
Two synthetic data sets, denoted A and B, are collected from the same hypothetical sample with different sampling grids. Grain centroids are calculated for both data sets. Pairs of matched grains are used to determine the transformation between A and B, then data set B is resampled on the sampling grid of data set A as described in Fig. 8. An IPF color legend is available in Fig. 5.

Figure 8
An algorithm to compute the rotation between sampling grids of two data sets, A and B, is provided. The centroid of grain i in data sets A and B is denoted (a_i^x, a_i^y, a_i^z) and (b_i^x, b_i^y, b_i^z), respectively. The least-squares affine transformation T is computed and used to map data set B to A with nearest-neighbor interpolation.
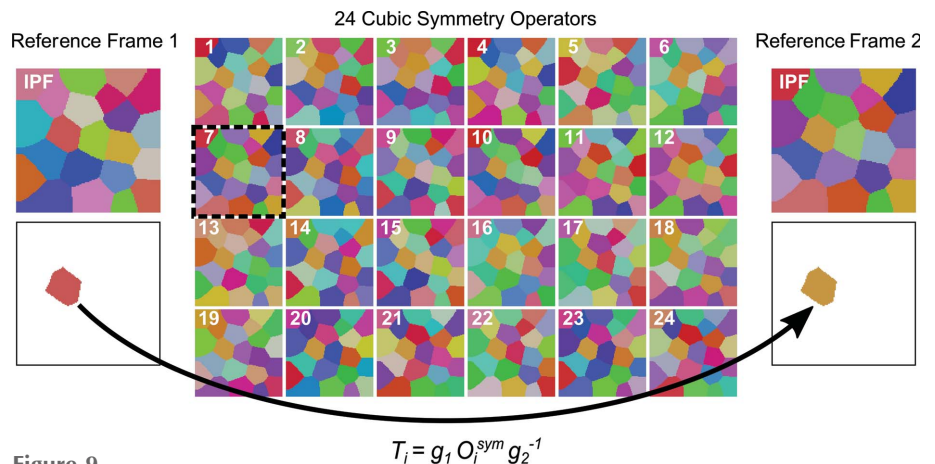

Figure 9
A small synthetic data set with orientations in two reference frames is shown in the top left (reference frame 1) and right (reference frame 2). The rotation between a single matched pair of grains (the red and orange pair shown in the bottom left and right) can be expressed in a different form for each crystal symmetry operator. The result of applying each of these transformations, T_i, to reference frame 1 is shown in the center. Notice that the red/orange pair from which T_i has been computed matches reference frame 2 for every case. However, the remaining grains are only aligned with the orientations in reference frame 2 for T_7.

volume, $(A_i \cap B_j)/(A_i \cup B_j)$ where A_i and B_j are the volumes of grain i and j in data sets A and B, respectively, is computed for every possible pair of grains between the data sets as a similarity metric. Grains are subsequently matched by descending metric value. If the orientation reference frames are aligned, an additional orientation match requirement can be imposed for pair assignment. A schematic of the process and a detailed description are provided in Figs. 11 and 12, respectively. Identification of matching grain pairs closes the alignment loop allowing iteration. Since both the sampling grid and the orientation reference frame alignment algorithms are uniquely dependent upon the grain pairs considered, convergence occurs when refining the alignment provides no new matched pairs.

Alignments for both sampling grids and orientation reference frames are performed iteratively, and sampling grid alignment requires nearest-neighbor interpolation. Repeated interpolation may introduce artifacts as seen in Fig. 4. In order to minimize these artifacts, transformations from consecutive alignment steps are combined and applied to the original volumes in a single interpolation step.

3. Results

Data sets were collected with both the DCT and TriBeam techniques for the same sample specimen as described in §2.1. These data sets were aligned in sample and orientation space, then resampled on the same grid to produce a merged data set containing voxelized information from both methods, as described in §2.3. At each voxel or for each grain the merged data set can be queried for the orientation information collected by each tomography experiment. In this section, the application of the data-set alignment and merging techniques is presented, followed by a quantification of the quality of fit of these algorithms, and finally metrics for comparison of the two data sets.
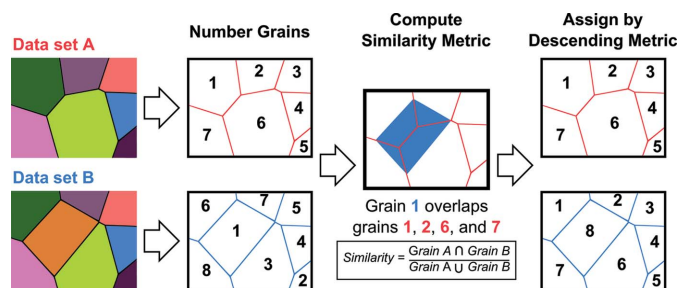
3.1. Combining data sets

Visualizations of the reconstructed DCT and TriBeam three-dimensional data sets, prior to merging, are shown in Fig. 13 using disorientation coloring (Patala *et al.*, 2012). This coloring was chosen for convenience so that grains close in orientation space are also close in coloring. The TriBeam data set is larger than the DCT data set along the z axis because more of the sample pillar volume was sampled during the TriBeam tomography experiment. Matching grain pairs by morphology alone is difficult and orientation coloring cannot be leveraged since the orientation reference frames are unaligned. However, since boundaries are colored by disorientation, pairs are readily identifiable, as shown in Fig. 14. The grains used to seed the alignment are shown in Fig. 15, and the resulting aligned and merged data sets are shown in Fig. 16. The transformation necessary for alignment of the orientation reference frames was the axis angle pair [0.3953, −0.9183, −0.0183] 3.1372 rad, or approximately 180° about [100] followed by 135° about [001], which is consistent with the

Require: list of matched grain pairs (grain A_i corresponds to grain B_i) and their average orientations
  for all grain pairs **do**
    $g_i \leftarrow$ rotation from B_i to A_i
    for all symmetry operators **do**
      $g_i' \leftarrow$ equivalent rotation
      apply g_i' to all other pairs
      for all other grain pairs **do**
        $g_j \leftarrow$ rotation from B_j to A_j
        for all symmetry operators **do**
          $g_j' \leftarrow$ equivalent rotation
          $\epsilon \leftarrow angle(g_j')$
        end for
        $\theta \leftarrow \min \epsilon$
      end for
      $\phi \leftarrow \bar{\theta}$
    end for
    $g \leftarrow g_i(\min \phi)$
  end for
  for all grains in data set B **do**
    apply $\bar{g}$
  end for

Figure 10
An algorithm to compute the rotation between crystal orientation reference frames of two data sets, A and B, is provided. The rotation is applied to the reference frame of data set B to align it with the reference frame of data set A.

Figure 11
The algorithm used to match grains between data sets is demonstrated for a simple example. Two synthetic data sets A and B are shown, one containing an additional grain. The grains in each data set are randomly numbered and then a similarity metric is calculated between all possible grain pairs. Pairs are subsequently matched by descending similarity. The similarity metric employed may be altered, allowing optimization of matching for different features. The details of this algorithm are described in Fig. 12.

Require: two sets of grain IDs (in the same sample reference frame) describing similar grains and their average orientations
  for all grains in data set A **do**
    for all grains in data set B **do**
      $m \leftarrow \frac{A_i \cap B_j}{A_i \cup B_j}$
      $\theta \leftarrow misorientation(A_i, B_j)$
      $pairs \leftarrow (i, j, m, \theta)$
    end for
  end for
  sort $pairs$ by descending m
  for all $pairs$ **do**
    if A_i is unmatched **and** B_j is unmatched **then**
      if $m > m_{threshold}$ **and** $\theta < \theta_{threshold}$ **then**
        assign B_j to A_i
      end if
    end if
  end for

Figure 12
An algorithm to match grain ID numbers of two data sets, A and B, is provided. An overlap metric is assigned for each possible grain pair, and grains in B are matched to grains in A by descending metric value.

sample being inverted between tomography experiments with a rotation about the pedestal axis. The affine transformation required to align the sampling grids was

$$\begin{bmatrix} -0.733 & -0.783 & -0.058 & -104.3 \\ -0.714 & -0.724 & 0.049 & -76.5 \\ 0.035 & 0.093 & -1.023 & -100.3 \\ 0 & 0 & 0 & 1 \end{bmatrix}.$$
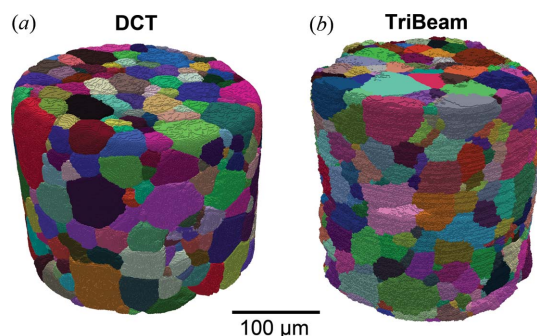
Extracting the rotation component of the affine transformation using singular value decomposition yields [0.3886, −0.9208, −0.0332] 3.0934 rad, a difference of 1° in axis and 2.5° in angle from the rotation required to align the orientation reference frames.
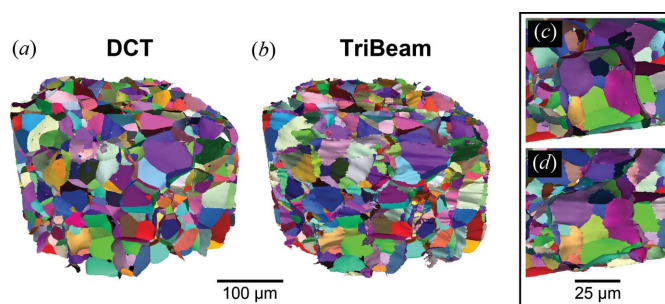
3.2. Quality of the merged data set

Three primary algorithms were used to combine the tomography data sets, addressing alignment of the orientation reference frame, alignment of the sampling grid and matching of grain pairs. For each algorithm a metric was selected to appraise performance.

The difference in centroid position of matched grain pairs is used as the metric for the sample alignment algorithm. A plot of the distance between the centroid positions for matched grain pairs in the DCT and TriBeam data sets is shown in Fig. 17. A small number of edge grains have displacements that are greater than 3–4 µm owing to a difference in the sensitivity of the tomography techniques to grains at the sample surface. The averages of the centroid displacements in the x, y and z positions are centered at 0.
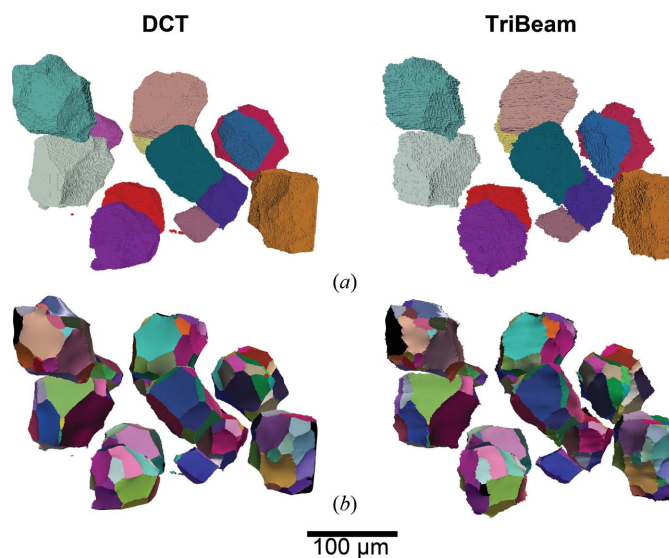
The difference in orientations between matching grain pairs in the two final time-step tomography data sets was used to assess the alignment of the orientation reference frames. Fig. 18 shows the difference in average orientation for each grain pair between the DCT and TriBeam tomography experiments. Most of the matched grain pairs have a difference that is between 0.25 and 0.75°, and all grain pairs have a

Figure 14
Grain boundary surface meshes of the DCT (*a*) and TriBeam (*b*) data sets are colored by Patala's disorientation coloring scheme (legend available in Fig. 5). This representation enables manual selection of grain pairs prior to alignment of the orientation reference frames as shown schematically in Fig. 6. Higher-magnification images of the grain boundaries from one corresponding grain pair are shown in (*c*) and (*d*), respectively.

Figure 15
Manually selected grain pairs from the DCT and TriBeam data sets are colored by grain average orientation (*a*) and boundary disorientation (*b*) after alignment. These grains were manually identified as described in §2.3.1 and used to initialize the alignment loop shown in Fig. 3. A disorientation color legend is available in Fig. 5.
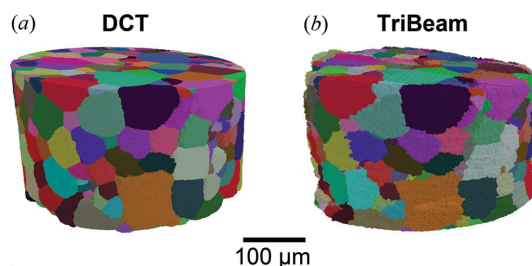

Figure 13
Reconstructions of the STO sample using data collected from the DCT experiment (*a*) and the TriBeam experiment (*b*) are shown. Grains are colored by their average orientation using a disorientation coloring scheme (Patala *et al.*, 2012). To color orientations with this scheme disorientations are computed with respect to identity. The orientation reference frames are not aligned, making selection of matching grain pairs difficult, even with the sampling grids coarsely aligned. Only careful morphological comparison can be used for matching. A disorientation color legend is available in Fig. 5.

Figure 16
Reconstructions of the DCT and TriBeam data sets are shown after alignment is complete. The two data sets are merged into one data container and grains matched so that data at any voxel or for any grain can be simultaneously probed from both tomography data sets. The data set is colored by disorientation with the legend available in Fig. 5.

difference less than 2.5°. There is a peak in orientation difference at 0.5°.

The similarity metric $(A_i \cap B_j)/(A_i \cup B_j)$ of matched grain pairs was selected to evaluate automated grain matching. Fig. 19 shows the distribution of similarity metrics observed. Most grain pairs have an overlap metric between 0.7 and 0.9. Pairs with small similarity metric generally correspond to grains that are fully contained in one volume but only partially captured by the other.

3.3. Direct voxelmetric data-set comparison

Accurately aligning the sampling grids allows for direct comparisons on a voxel-by-voxel basis. This type of analysis is useful to make grain-independent comparisons, such as orientation gradients, boundary locations and measures of reconstruction or confidence. The reconstructions of DCT and TriBeam data sets have been sliced orthogonally in Fig. 20 to show the relative spatial positions of the identical grains. Voxels for which the disorientation angle between the two data sets is below 5° are transparent. Any voxels with higher angles are displayed using the disorientation coloring scheme described earlier (Patala *et al.*, 2012). Therefore, the colored regions indicate differences in orientation assignment between the DCT and TriBeam reconstructions that have a disor-

ientation greater than 5°, accounting for 20% of the voxels. Half of these voxels correspond to boundary discrepancies with a typical thickness of 1–3 μm, and the balance of the voxels arise from unresolved grains in the DCT reconstruction.

3.4. Direct grain-to-grain comparison

The grains in each data set were matched using a grain numbering algorithm for continuous voxel regions which shared orientations within a 5° tolerance, as described in §2.3.4. Of particular interest are the unique grains, which only exist in one of the two data sets and were not matched. Visualizations of the grains that are unique to either the DCT or the TriBeam data set are shown in Fig. 21. Unique grains detected by the TriBeam are plotted in Fig. 22. The unique grains resolved by the TriBeam are predominantly either (i) larger and located at the sample surface or (ii) smaller grains below the resolution limit of this DCT reconstruction. Slices from the merged three-dimensional data sets were made, showing examples of cases (i) and (ii) in Fig. 23. From the merged data-set volume, 159 unique grains were found exclusively in the TriBeam data set (of 741 total grains), which can be attributed to the grains being either below the DCT reconstruction's resolution limit, apparent in Fig. 24, or high aspect ratio grains on the sample exterior.

The unique grains in the DCT data set predominantly share at least one low-angle grain boundary (below 1.5°) with a neighboring grain. EBSD data collected by the TriBeam technique at these low-angle boundaries were not segmented into individual grains owing to the variability in orientation measurements. However, the implementation of additional grain boundary definition (segmentation) algorithms may enable more accurate reconstruction of subgrains for this data set. EBSD measurement variability can be introduced by a wide range of factors, including diffraction pattern indexing, EBSD camera binning and exposure times, spread in energy of electrons used in diffraction, surface roughness, intrinsic grain orientation substructure, and electron beam sampling volume effects. Examples of grains that were not segmented and matched to a grain in the DCT data set are shown in Fig. 25. Of the 606 total grains collected by DCT from the merged data-
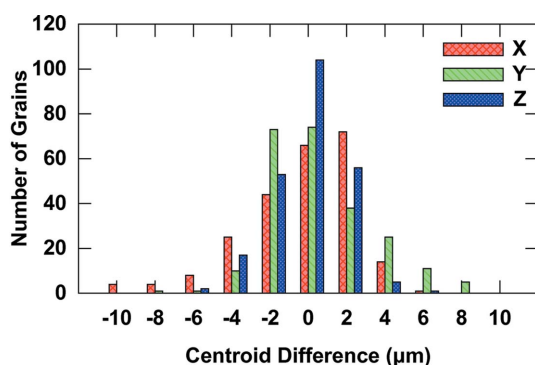

Figure 17
A histogram of difference in TriBeam centroid positions relative to corresponding DCT centroids is shown. The average of all the centroid positions along each primary axis is 0.
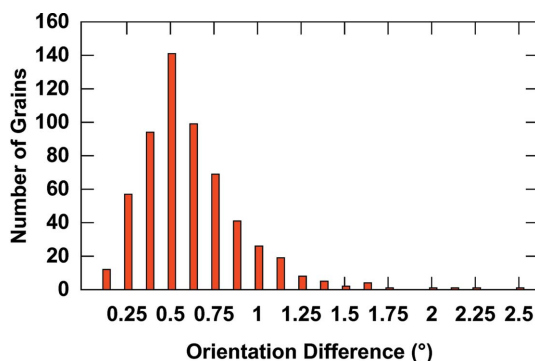

Figure 18
A histogram of disorientation angle between matched grain pairs in the DCT and TriBeam tomography data sets is shown. Most grain pairs exhibit an angle of between 0.25 and 0.75°.
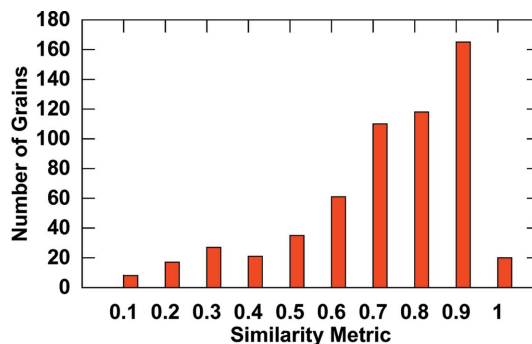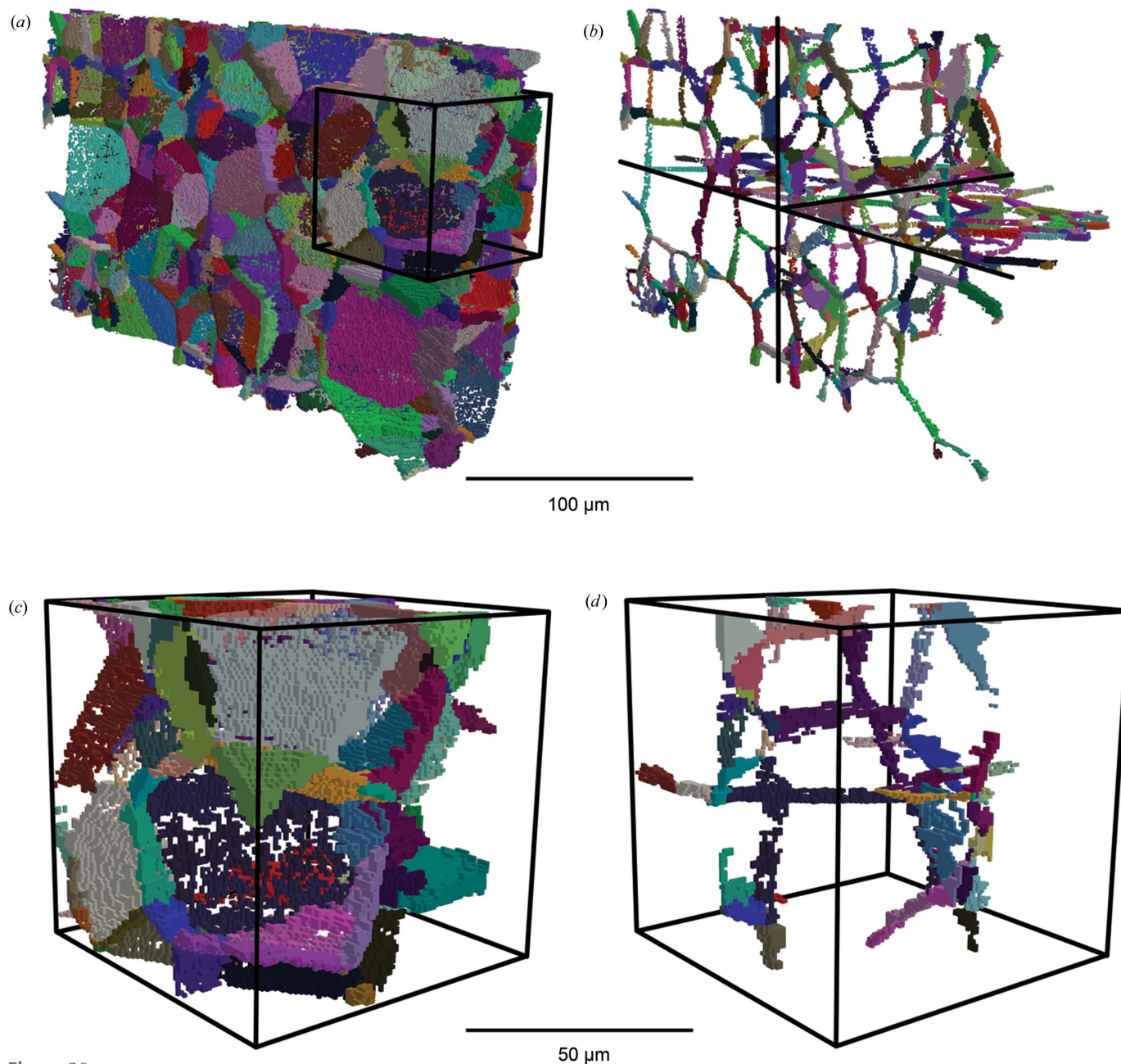

Figure 19
A histogram of the similarity metric $(A_i \cap B_j)/(A_i \cup B_j)$ for all matched grain pairs between the DCT and TriBeam data sets is plotted. The lowest similarity metric values correspond to grains that were not fully contained in the overlapping tomography data-set volume.

9

set volume, 24 unique grains were found only in the DCT data set, mostly having low-angle grain boundaries.

4. Discussion

Synchrotron X-ray DCT analysis of STO samples has the ability to provide time-resolved structural information which can inform grain growth mechanisms and simulation. In this work, the advantages of both the DCT and TriBeam techni-

ques are leveraged by complementing four-dimensional grain evolution data with sub-micrometre resolution on the final time step. Although a resolution limit exists for the type of DCT experiment performed in this work, it may be improved by performing higher resolution DCT experiments using different synchrotron beamlines, *e.g.* a nanotomography beamline (Withers, 2007). Similarly, multiple time steps provide an opportunity to observe shrinking grains before they fall below the resolution limit.

Figure 20
A grain difference map is rendered for half the pedestal (*a*) and three 2.8 µm-thick orthogonal sections (*b*). For each voxel, disorientation is computed between the orientation of the assigned DCT grain and the average orientation of the assigned TriBeam grain. If the disorientation angle is below 5° the voxel is transparent, otherwise it is colored by disorientation. A higher magnification of the inset indicated in (*a*) is shown in (*c*) with corresponding orthogonal sections in (*d*). Colored regions with a perforated appearance, *e.g.* the dark-blue face in (*c*), indicate voxel-level agreement in grain boundary location between the two data sets. A disorientation color legend is available in Fig. 5.

The direct comparison of TriBeam with DCT data sets on a grain-by-grain and voxel-by-voxel basis has provided a means of evaluating the accuracy of the experimental tomographic data collection techniques and the data reconstruction algorithms. Qualitatively, a difference in boundary locations is observed in Fig. 20. The plot shown in Fig. 24 and the reconstructed grains shown in Fig. 22 indicate that the smallest resolvable grains for this type of DCT reconstruction are between 10 and 20 µm, given the imaging parameters and specimen employed. The DCT reconstructions show similar grain topological information to that collected with the TriBeam, as shown in Fig. 15, for a selection of large-diameter grains.

When collecting three-dimensional EBSD data, such as those from the TriBeam, variability in orientation measurements at each sampling point scales inversely with collection time. For example, the resolution of an orientation measurement can be refined by collecting a larger electron diffraction pattern image or by using a longer camera exposure time. Therefore, grains with very low angle boundaries (less than $1.5°$), such as many of those shown in Fig. 21(a), may not be easily resolved from their neighbors using the EBSD parameters in this TriBeam data set. However, EBSD can be used to collect data from materials which have large internal orientation gradients due to dislocation substructure (Konrad *et al.*, 2006; Britton *et al.*, 2013).
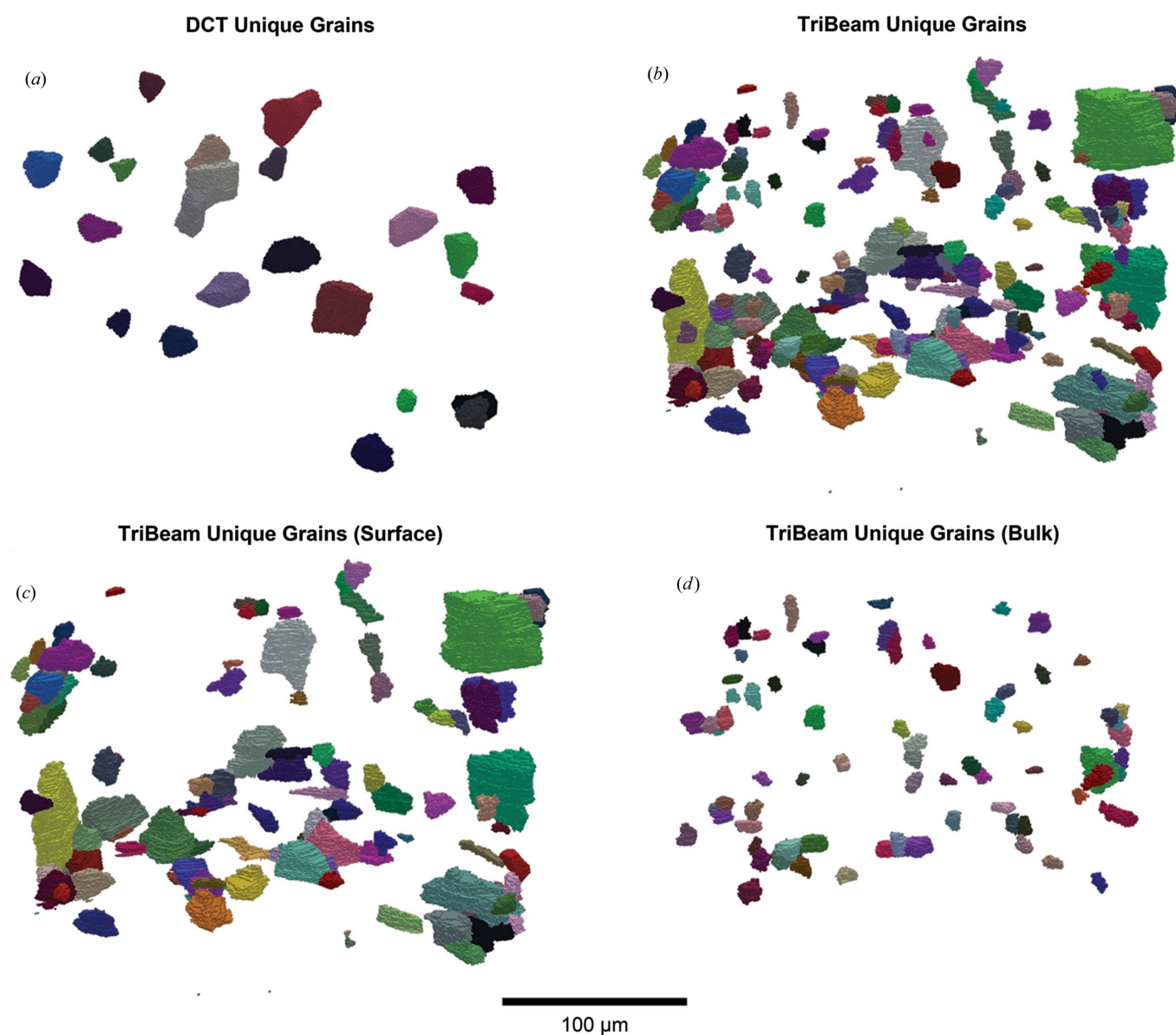

Figure 21
Unique grains in the DCT (*a*) and TriBeam (*b*) data sets are shown. The total volume of the unmatched TriBeam grains (*b*) comprises 3.8% of the matched volume. Most unmatched grains in the DCT data set correspond to segmentation errors in the TriBeam volume. If two grains are erroneously merged during TriBeam segmentation, one will be left unpaired in the DCT volume. Most unmatched grains in the TriBeam data set are unresolved in the DCT data set. Unique grains in the TriBeam data set which touch the surface (*c*) may be larger but are generally thin in the radial direction. Internal grains (*d*) are predominantly small and equiaxed. A disorientation color legend is available in Fig. 5.
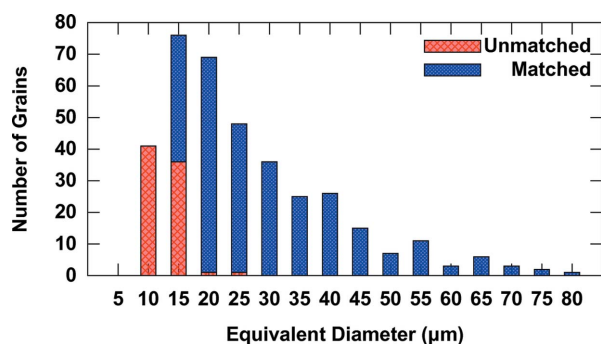
Figure 22
A histogram of equivalent diameter for grains reconstructed in the TriBeam data set is shown. The majority of the unmatched grains do not exist in the DCT data set, presumably because too few diffraction spots were available for DCT reconstruction. These cases may correspond to spot overlap or resolution limits.
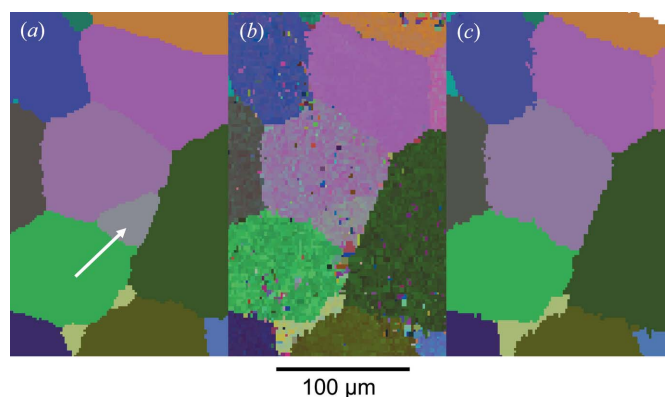

Figure 25
The same region is colored by DCT grain average orientation (*a*), TriBeam voxel orientation (*b*) and TriBeam grain average orientation (*c*). The EBSD segmentation algorithm erroneously merges neighboring grains with a low disorientation connection (below 1.5°). A disorientation color legend is available in Fig. 5.

The methodology for merging of tomographic data sets used in this research can be applied generally to align data sets containing orientation data and/or spatial data with automated microstructural feature matching. The output of the alignment process can be used to quantitatively compare two-dimensional and three-dimensional data sets using data from a wide range of imaging modalities and spatial resolutions. Future applications could include the alignment and merger of tomographic data sets at different length scales and timescales.
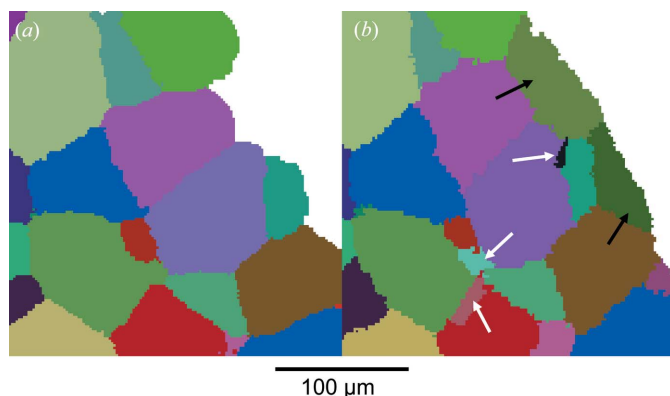

Figure 23
The same region is colored by grain average orientation for the DCT (left) and TriBeam (right) data sets. Very small internal or thin surface grains, indicated by white and black arrows, respectively, are often unresolved in the DCT reconstruction. A disorientation color legend is available in Fig. 5.
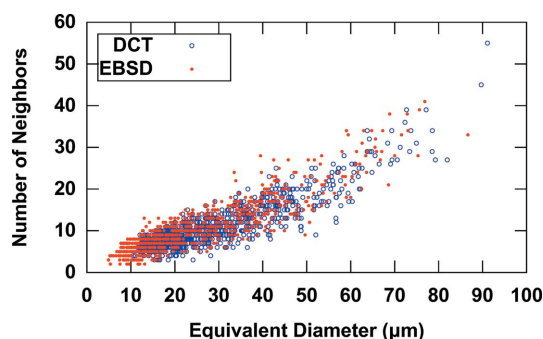
5. Conclusions

Nondestructive and destructive three-dimensional tomographic techniques have been combined to produce a merged data set which can be compared on a voxel-by-voxel basis. The methods used to merge the data sets have implications for use in creating unified data sets that contain multiple imaging modalities on a consistent spatial reference frame. In this work, we show the combination of high angular precision diffraction data with high spatial precision EBSD data, which provides (i) a route for improvement of X-ray reconstruction algorithms and (ii) a means of directly linking the extensive set of microanalysis tools available *via* serial sectioning techniques with four-dimensional (time-resolved) X-ray data sets.

In summary, a TriBeam serial sectioning three-dimensional reconstruction was successfully merged with a DCT reconstruction to create a combined three-dimensional data set. This merger required development of algorithms for union of the sampling grids, alignment of crystal orientation reference frame and automated grain matching. These algorithms are robust and flexible, lending themselves to similar mergers for varied imaging modalities. Alignment enables augmentation of ensemble measures with direct quantitative voxel- and grain-level comparisons revealing the following:

(i) 95% of the matched grain pairs have differences in centroid locations that are within 4 µm.

Figure 24
Equivalent diameters for all grains in the DCT and TriBeam data sets are plotted against their number of neighbors. The spatial resolution of the TriBeam extends below that of the DCT technique for the experimental parameters used. On average, matched DCT grains have a 0.2 µm larger equivalent diameter and 0.74 fewer neighbors than their TriBeam counterparts. The grains from the TriBeam data set that are unmatched and have an equivalent diameter less than 12 µm account for only 0.35% of the total matched volume. This result is consistent with merging small, unresolved grains into their neighbors.

12

(ii) For the imaging and sample conditions employed, grains not captured by the DCT reconstruction method usually have an equivalent diameter below 10–12 µm.

(iii) The number of neighbors scales with grain size in the merged data set.

(iv) Within the merged data-set volume, 741 total grains were reconstructed by the TriBeam with 159 unique (unmatched) grains, and 606 total grains were reconstructed by DCT with 24 unique grains.

(v) In total, 582 grain pairs were matched within the merged sample volume.

(vi) Large grains not captured *via* DCT were primarily located at the radial boundary of the sample pedestal.

(vii) For the EBSD imaging and sample conditions employed, grains not captured by the TriBeam usually have a low-angle grain boundary.

References

Bäurer, M., Kungl, H. & Hoffmann, M. J. (2009). *J. Am. Ceram. Soc.* **92**, 601–606.

Bäurer, M., Weygand, D., Gumbsch, P. & Hoffmann, M. J. (2009). *Scr. Mater.* **61**, 584–587.

Britton, T. B., Jiang, J., Clough, R., Tarleton, E., Kirkland, A. I. & Wilkinson, A. J. (2013). *Ultramicroscopy*, **135**, 126–135.

Cloetens, P., Pateyron-Salomé, M., Buffiere, J. Y., Peix, G., Baruchel, J., Peyrin, F. & Schlenker, M. (1997). *J. Appl. Phys.* **81**, 5878–5886.

Echlin, M. P., Lenthe, W. C., Stinville, J. C., Wielewski, E., Dawson, P., Miller, M. & Pollock, T. M. (2014). *TriBeam Tomography of Ti6-4 for Plasticity Characterization*, TMS Annual Meeting. Hoboken: TMS.

Echlin, M. P., Mottura, A., Torbet, C. J. & Pollock, T. M. (2012). *Rev. Sci. Instrum.* **83**, 023701.

Echlin, M. P., Mottura, A., Wang, M., Mignone, P. J., Riley, D. P., Franks, G, V. & Pollock, T. M. (2014). *Acta Mater.* **64**, 307–315.

Echlin, M. P., Straw, M., Randolph, S., Filevich, J. & Pollock, T. M. (2015). *Mater. Characterization*, **100**, 1–12.

Gonzalez, D., King, A., Mostafavi, M., Reischig, P., Rolland du Roscoat, S., Ludwig, W., Quinta da Fonseca, J., Withers, P. J. & Marrow, T. J. (2013). *Acta Mater.* **61**, 7521–7533.

Gower, J. C. & Dijksterhuis, G. B. (2004). *Procrustes Problems*. Oxford University Press.

Groeber, M. & Jackson, M. (2014). *Integr. Mater. Manuf. Innov.* **3**, 5.

Johnson, G., King, A., Honnicke, M. G., Marrow, J. & Ludwig, W. (2008). *J. Appl. Cryst.* **41**, 310–318.

Kak, A. C. & Slaney, M. (1988). *Principles of Computerized Tomographic Imaging*. New York: IEEE Press.

Kammers, A. D. & Daly, S. (2013). *Exp. Mech.* **53**, 1743–1761.

King, A., Herbig, M., Ludwig, W., Reischig, P., Lauridsen, E. M., Marrow, T. & Buffiére, J. Y. (2010). *Nucl. Instrum. Methods Phys. Res. Sect. B*, **268**, 291–296.

Konrad, J., Zaefferer, S. & Raabe, D. (2006). *Acta Mater.* **54**, 1369–1380.

Ludwig, W., King, A., Reischig, P., Herbig, M., Lauridsen, E. M., Schmidt, S., Proudhon, H., Forest, S., Cloetens, P., Rolland du Roscoat, S., Buffiére, J. Y., Marrow, T. J. & Poulsen, H. F. (2009). *Mater. Sci. Eng. A*, **524**, 69–76.

Ludwig, W., Reischig, P., King, A., Herbig, M., Lauridsen, E. M., Johnson, G., Marrow, T. J. & Buffiére, J. Y. (2009). *Rev. Sci. Instrum.* **80**, 033905.

Ludwig, W., Schmidt, S., Lauridsen, E. M. & Poulsen, H. F. (2008). *J. Appl. Cryst.* **41**, 302–309.

Nervo, L., King, A., Wright, J. P., Ludwig, W., Reischig, P., Quinta da Fonseca, J. & Preuss, M. (2014). *J. Appl. Cryst.* **47**, 1402–1416.

Nolze, G. (2007). *Ultramicroscopy*, **107**, 172–183.

Patala, S., Mason, J. K. & Schuh, C. A. (2012). *Prog. Mater. Sci.* **57**, 1383–1425.

Poulsen, H. F., Nielsen, S. F., Lauridsen, E. M., Schmidt, S., Suter, R. M., Lienert, U., Margulies, L., Lorentzen, T. & Juul Jensen, D. (2001). *J. Appl. Cryst.* **34**, 751–756.

Reischig, P., King, A., Nervo, L., Viganó, N., Guilhem, Y., Palenstijn, W. J., Batenburg, K. J., Preuss, M. & Ludwig, W. (2013). *J. Appl. Cryst.* **46**, 297–311.

Rowenhorst, D. (2013). *Microsc. Microanal.* **19** (Suppl. S2), 840–841.

Schmidt, S. (2014). *J. Appl. Cryst.* **47**, 276–284.

Stinville, J. C., Echlin, M. P., Texier, D., Bridier, F., Bocher, B. & Pollock, T. M. (2015). *Exp. Mech*. In the press.

Sutton, M. A., Li, N., Garcia, D., Cornille, N., Orteu, J. J., McNeill, S. R., Schreier, H. W. & Li, X. (2006). *Meas. Sci. Technol.* **17**, 2613–2622.

Syha, M., Bäurer, M., Rheinheimer, W., Ludwig, W., Lauridsen, E. M., Weygand, D. & Gumbsch, P. (2012). *Developments in Strategic Materials and Computational Design III*, pp. 127–137. Hoboken: John Wiley and Sons.

Syha, M., Rheinheimer, W., Bäurer, M., Lauridsen, E. M., Ludwig, W., Weygand, D. & Gumbsch, P. (2012). *Scr. Mater.* **66**, 1–4.

Syha, M., Trenkle, A., Lödermann, B., Graff, A., Ludwig, W., Weygand, D. & Gumbsch, P. (2013). *J. Appl. Cryst.* **46**, 1145–1150.

Titus, M. S., Echlin, M. P., Gumsch, P. & Pollock, T. M. (2015). *J. Appl. Phys.* Submitted.

Withers, P. J. (2007). *Mater. Today*, **10**, 26–34.

Wright, S. I. & Nowell, M. M. (2006). *Microsc. Microanal.* **12**, 72–84.

Wu, Z. & Sullivan, J. M. (2003). *Int. J. Numer. Methods Eng.* **58**, 189–207.

1046   William C. Lenthe *et al.* · Comparison of TriBeam and DCT STQ data sets   *J. Appl. Cryst.* (2015). **48**, 1034–1046

13